



ALMA-LEGUS. II. The Influence of Subgalactic Environments on Molecular Cloud Properties

Molly K. Finn¹ , Kelsey E. Johnson¹ , Remy Indebetouw^{1,2} , Allison H. Costa² , Angela Adamo³ , Alessandra Aloisi⁴ , Lauren Bittle⁵ , Daniela Calzetti⁶ , Daniel A. Dale⁷ , Clare L. Dobbs⁸ , Jennifer Donovan Meyer² , Bruce G. Elmegreen⁹ , Debra M. Elmegreen¹⁰ , Michele Fumagalli^{11,12} , J. S. Gallagher^{13,14} , Kathryn Grasha^{15,16,17} , Eva K. Grebel¹⁸ , Robert C. Kennicutt^{19,20} , Mark R. Krumholz^{15,16} , Janice C. Lee⁴ , Matteo Messa^{3,21} , Preethi Nair²² , Elena Sabbi⁴ , Linda J. Smith⁴ , David A. Thilker²³ , Bradley C. Whitmore⁴ , and Aida Wofford²⁴

¹ Department of Astronomy, University of Virginia, Charlottesville, VA 22904, USA; mf4yu@virginia.edu

² National Radio Astronomy Observatory, 520 Edgemont Road, Charlottesville, VA 22903, USA

³ Department of Astronomy, The Oskar Klein Centre, Stockholm University, SE-106 91 Stockholm, Sweden

⁴ Space Telescope Science Institute, 3700 San Martin Drive, Baltimore, MD 21218, USA

⁵ Independent Researcher, USA

⁶ Department of Astronomy, University of Massachusetts Amherst, 710 North Pleasant Street, Amherst, MA 01003, USA

⁷ Department of Physics & Astronomy, University of Wyoming, Laramie, WY 82071, USA

⁸ School of Physics and Astronomy, University of Exeter, Stocker Road, Exeter, EX4 4QL, UK

⁹ IBM Research Division, T.J. Watson Research Center, 1101 Kitchawan Road, Yorktown Heights, NY 10598, USA

¹⁰ Department of Physics and Astronomy, Vassar College, Poughkeepsie, NY 12604, USA

¹¹ Dipartimento di Fisica G. Occhialini, Università degli Studi di Milano Bicocca, Piazza della Scienza 3, I-20126 Milano, Italy

¹² INAF—Osservatorio Astronomico di Trieste, via G.B. Tiepolo 11, I-34143 Trieste, Italy

¹³ Department of Astronomy, University of Wisconsin—Madison, 475 North Charter Street, Madison, WI 53706, USA

¹⁴ Department of Physics and Astronomy, Macalester College, 1600 Grand Avenue, Saint Paul, MN 55105, USA

¹⁵ Research School of Astronomy and Astrophysics, Australian National University, Cotter Road, Weston ACT 2612, Australia

¹⁶ ARC Centre of Excellence for Astrophysics in 3D (ASTRO-3D), Canberra ACT 2600, Australia

¹⁷ Visiting Fellow, Harvard-Smithsonian Center for Astrophysics, 60 Garden Street, Cambridge, MA 02138, USA

¹⁸ Astronomisches Rechen-Institut, Zentrum für Astronomie der Universität Heidelberg, Mönchhofstrasse 12–14, D-69120 Heidelberg, Germany

¹⁹ Steward Observatory, University of Arizona, Tucson, AZ 85719, USA

²⁰ George P. and Cynthia W. Mitchell Institute for Fundamental Physics and Astronomy, Texas A&M University, College Station, TX 77845, USA

²¹ Observatoire de Genève, Université de Genève, Versoix, Versoix, Switzerland

²² Department of Physics and Astronomy, The University of Alabama, Tuscaloosa, AL 35487, USA

²³ Department of Physics and Astronomy, The Johns Hopkins University, Baltimore, MD, 21218 USA

²⁴ Instituto de Astronomía, Universidad Nacional Autónoma de México, Unidad Académica en Ensenada, Km 103 Carretera Tijuana–Ensenada, Ensenada, B.C., C.P. 22860, Mexico

Received 2023 August 25; revised 2023 December 26; accepted 2023 December 27; published 2024 March 12

Abstract

We compare the molecular cloud properties in subgalactic regions of two galaxies, barred spiral NGC 1313, which is forming many massive clusters, and flocculent spiral NGC 7793, which is forming significantly fewer massive clusters despite having a similar star formation rate to NGC 1313. We find that there are larger variations in cloud properties between different regions within each galaxy than there are between the galaxies on a global scale, especially for NGC 1313. There are higher masses, line widths, pressures, and virial parameters in the arms of NGC 1313 and the center of NGC 7793 than in the interarm and outer regions of the galaxies. The massive cluster formation of NGC 1313 may be driven by its greater variation in environment, allowing more clouds with the necessary conditions to emerge, although no one parameter seems primarily responsible for the difference in star formation. Meanwhile NGC 7793 has clouds that are as massive and have as much kinetic energy as the clouds in the arms of NGC 1313, but have densities and pressures more similar to those in the interarm regions and so are less inclined to collapse and form stars. The cloud properties in NGC 1313 and NGC 7793 suggest that spiral arms, bars, interarm regions, and flocculent spirals each represent distinct environments with regard to molecular cloud populations. We see surprisingly little difference in surface density between the regions, suggesting that the differences in surface densities frequently seen between arm and interarm regions in lower-resolution studies are indicative of the sparsity of molecular clouds, rather than differences in their true surface density.

Unified Astronomy Thesaurus concepts: Young star clusters (1833); Interstellar medium (847); Molecular clouds (1072); Star formation (1569); Spiral galaxies (1560)

1. Introduction

Spiral galaxies are home to the majority of local star formation (Brinchmann et al. 2004), and so it is important for us to

understand how the environments of different regions within the galaxies and different types of spiral galaxies affect star formation. The molecular gases in bars, spiral arms, interarm regions, and galaxy centers all experience different conditions, which can in turn influence the star formation taking place in each environment.

Much work has been done on understanding how spiral density waves and stellar feedback impact cloud formation, collapse, and dispersal, both from simulations and from



Original content from this work may be used under the terms of the [Creative Commons Attribution 4.0 licence](https://creativecommons.org/licenses/by/4.0/). Any further distribution of this work must maintain attribution to the author(s) and the title of the work, journal citation and DOI.

observations. There have been several surveys to study the molecular gas in nearby spiral galaxies at the scale of giant molecular clouds (GMCs), such as PAWS (the PdBI Arcsecond Whirlpool Survey), which mapped M51 in CO(1–0) at 40 pc resolution (Schinnerer et al. 2013); CANON (CARMA and Nobeyama Nearby Galaxies), which mapped the inner disks of nearby spiral galaxies in CO(1–0) and enabled a focused study of molecular cloud properties using a subsample at 62–78 pc resolution (Donovan Meyer et al. 2013); PHANGS-ALMA (Physics at High Angular Resolution in Nearby Galaxies–Atacama Large Millimeter/submillimeter Array), which mapped 90 galaxies in CO(2–1) at ~ 100 pc resolution (Leroy et al. 2021); and most recently the mapping of the barred spiral galaxy M83 in CO(1–0) at 40 pc resolution (Koda et al. 2023).

These studies have consistently shown that at ~ 40 – 100 pc resolutions, the molecular gas in the spiral arms tends to be brighter and have higher surface densities, velocity dispersions, and pressures than the gas in interarm regions, especially when a strong bar is present (Colombo et al. 2014; Sun et al. 2018, 2020; Rosolowsky et al. 2021; Koda et al. 2023). They have also shown that the slope of the distribution of cloud masses is shallower and truncates at higher masses in the spiral arms than in the interarm regions (Rosolowsky et al. 2008; Koda et al. 2009; Colombo et al. 2014), but that despite the greater amount of star formation in the arms, the depletion time there is not significantly shorter (Querejeta et al. 2021). Rather, Yu et al. (2021) found that the depletion time of the gas is more closely related to the strength of the spiral arms, with stronger arms being associated with shorter depletion times and higher specific star formation rates (SFRs).

These observations are well modeled by simulations, especially those of grand-design spiral galaxies. Simulations also find that the spiral arms are generally the sites of active star formation rather than the interarm regions (Dobbs et al. 2014), and that GMCs are assembled in the spiral arms and are then sheared into smaller clouds in the interarm regions, resulting in lower-mass clouds being found in these regions (Dobbs & Pringle 2013). The breaking up of massive clouds via shear aligns well with measurements of the lifetimes of clouds in the interarm regions of M51 (Meidt et al. 2015) and M83 (Koda et al. 2023). Massive clouds are expected to be denser and have longer lifetimes, allowing them to form more massive clusters in the spiral arms before they are dispersed (Dobbs et al. 2011, 2017). Meidt et al. (2013) proposed that the higher amount of streaming motion in the interarm regions relative to the arms stabilizes the clouds and suppresses collapse.

Pettitt et al. (2020) found that the cause of the spiral pattern (e.g., density waves, interaction, or underlying gravitational instability) has no effect on the simulated GMC properties. However, GMCs have a shallower mass distribution with more massive clouds after the galaxy experiences a tidal flyby, especially in the spiral arms, and many of the clouds become unbound during this process (Nguyen et al. 2018; Pettitt et al. 2018).

In flocculent spiral galaxies, the distinction between interarm and arm regions is less robust, but Dobbs et al. (2019) still found a difference in the steepness of the cloud mass distribution, where star-forming clouds have a shallower mass distribution than non-star-forming clouds, similar to the difference between arm and interarm regions in grand-design galaxies. However, Dobbs et al. (2018) found that to simulate a

flocculent spiral with a weak spiral structure, the stellar feedback must be higher than in a galaxy with strong spirals.

These differences in cloud properties have important repercussions not just for where in the galaxy stars form, but also for what kinds of stars and star clusters form. Measurements of the cluster formation efficiency, defined by Adamo et al. (2015) as the fraction of stars that form in clusters, indicate that it is correlated with the surface density of the gas (Adamo et al. 2011, 2015, 2020; Silva-Villa et al. 2013; Johnson et al. 2016).

Furthermore, the maximum mass of star clusters, where the mass distribution truncates, appears to depend on the SFR surface density of the galaxy (Adamo et al. 2015; Johnson et al. 2017; Messa et al. 2018; Wainer et al. 2022). A more extreme version of this trend has been seen in starburst environments that form massive super star clusters, such as the Antennae galaxies, where clouds have been measured to have extremely high pressures and surface densities (Johnson et al. 2015; Sun et al. 2018; Finn et al. 2019; Krahm et al. 2024). The hierarchical clustering of the molecular gas also appears to imprint its structure on the spatial clustering of the star clusters, with implications for their evolution and their potential for dispersal (Grasha et al. 2017a, 2017b, 2018; Menon et al. 2021; Turner et al. 2022).

In this paper, we build on the analysis of Finn et al. (2024, hereafter referred to as Paper I) to further our understanding of how different galactic environments influence the conditions and outcomes of star formation. We use for comparison two galaxies from the Legacy ExtraGalactic UV Survey (LEGUS; Calzetti et al. 2015): barred spiral NGC 1313 and flocculent spiral NGC 7793. These galaxies have similar masses (2.6×10^9 and $3.2 \times 10^9 M_\odot$; Calzetti et al. 2015), metallicities ($12 + \log(\text{O}/\text{H}) = 8.4$ and 8.52 ; Walsh & Roy 1997; Stanghellini et al. 2015), and SFRs (1.15 and $0.52 M_\odot \text{ yr}^{-1}$; Calzetti et al. 2015). However, in Paper I we demonstrated that NGC 1313 hosts significantly more star clusters than NGC 7793 as identified by LEGUS, especially young, massive clusters, even after correcting for their small difference in SFR (see Figure 1). The similarities of the galaxies, including their similarity in distance (4.6 and 3.7 Mpc; Radburn-Smith et al. 2011; Gao et al. 2015; Qing et al. 2015; Sabbi et al. 2018), make the pair an excellent laboratory for directly comparing how the molecular gas conditions and galactic structure affect star cluster formation. For a more detailed description of these two galaxies, their properties, and their larger environments, see Paper I.

In Paper I, we found surprisingly minimal differences in the cloud properties when comparing the two galaxies as a whole. NGC 1313 had slightly higher surface densities, higher external pressures, and shorter freefall times than NGC 7793. The clouds in NGC 1313 also had higher kinetic energies per spatial scale when fitting a power law to the size–line width relation, and more clouds were near virial equilibrium there than in NGC 7793. However, the clouds with virial parameters near 1 were not any more spatially correlated with the locations of star clusters than the general cloud population in either galaxy.

We expand this previous analysis by considering how the subgalactic environments affect the molecular cloud populations and how those relate to the cluster formation occurring in those regions. We split NGC 1313 into four regions: the bar, northern arm, southern arm, and interarm. In NGC 7793, the spiral arms are too weak for robust delineations of arm and interarm, so we instead split the galaxy into regions by galactocentric radius.

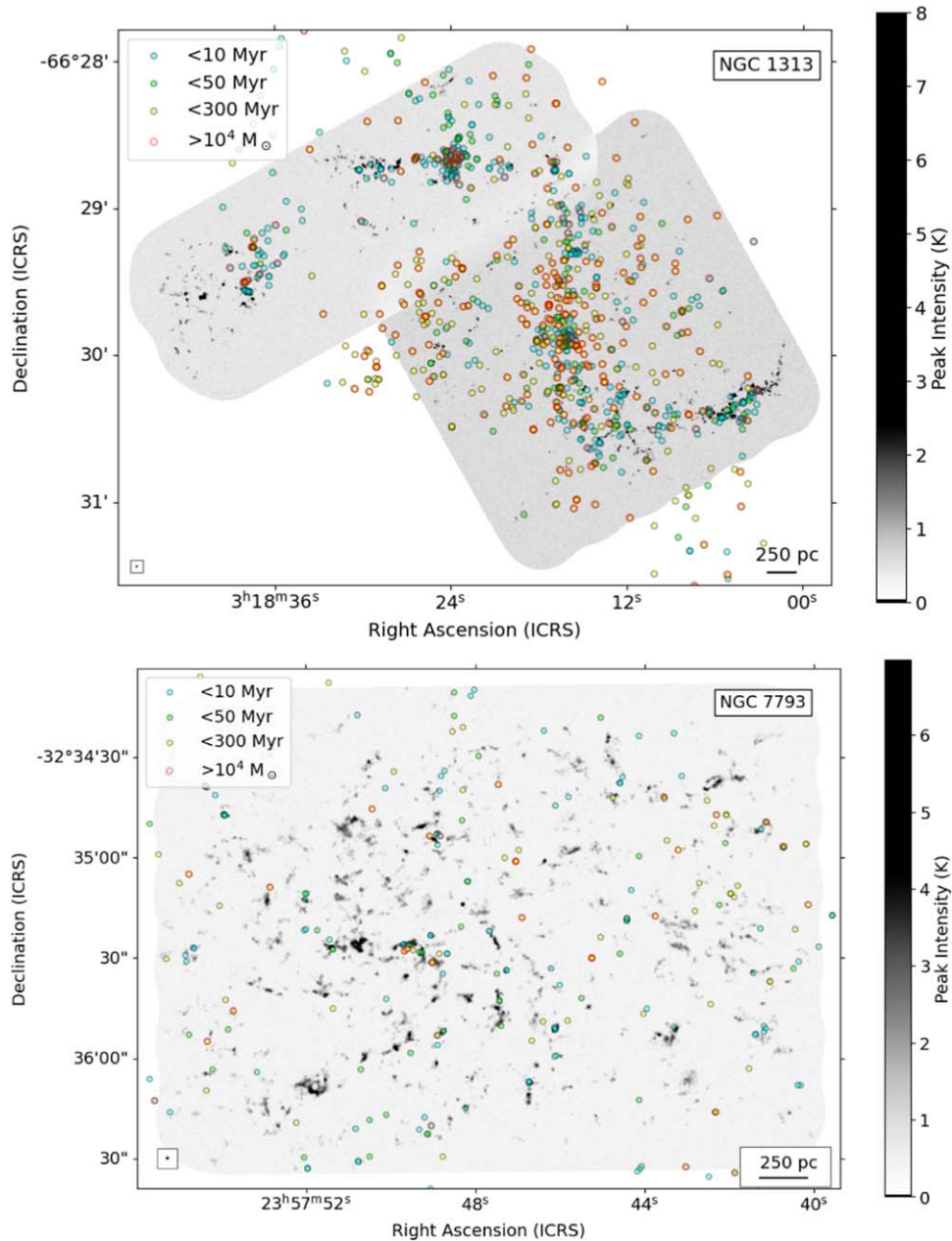


Figure 1. Peak intensity maps of CO(2–1) from Paper I in gray scale, overlaid with the positions of clusters identified in the LEGUS catalogs for NGC 1313 (top) and NGC 7793 (bottom). The beam sizes of 13 pc are shown in the bottom left corner. The clusters are colored by age with clusters younger than 10 Myr in cyan, clusters aged 10–50 Myr in green, and clusters aged 50–300 Myr in yellow. Clusters that are more massive than $10^4 M_{\odot}$ are outlined in red. NGC 1313 has significantly more star clusters overall than NGC 7793, and especially has more red-outlined massive star clusters, both by number and by fraction of the total cluster mass.

These regions are described in Section 2, along with the observations, the cloud structures, and their properties we use from Paper I. In Section 3 we describe the cluster catalogs used from LEGUS. We examine the size–line width relation of clouds in each region in Section 4, and the virialization of those clouds in Section 5. We then compare the distributions of all the different cloud properties and different galactic regions in Section 6. We discuss our results in Section 7 and then summarize the primary findings in Section 8.

2. Observations

2.1. CO(2–1)

Both galaxies have been observed by ALMA (project code 2015.1.00782.S; PI: K. E. Johnson) using Band 6 covering the

Table 1
ALMA $^{12}\text{CO}(2-1)$ Observations

Galaxy	Beam (arcsec)	Beam (pc)	rms (K)	Velocity Resolution (km s^{-1})
NGC 1313	0.58	13	0.15	1.33
NGC 7793	0.72	13	0.2	1.33

$^{12}\text{CO}(2-1)$ line with the 12 m array. The details of these observations, the data reduction, and the imaging process are discussed in Paper I, with the parameters of the final images shown in Table 1, reproduced from Paper I. Figure 1 shows the peak intensity maps of these observations, overlaid with the positions of clusters identified by LEGUS.

In this study, we use the clumps and dendrogram structures identified in Section 4 of Paper I using `quickclump` (Sidorin 2017) and `astrodendro` (Rosolowsky et al. 2008), as well as all the properties calculated for these structures in Paper I as described in Section 5 and published in the tables of the appendix in that paper. These properties include the mass (M), radius (R), velocity dispersion (σ_v), virial parameter (α_{vir}), surface density (Σ), external pressure (P_e), and freefall time (t_{ff}).

Dendrograms are hierarchical and include substructure at many size scales, and so are preferred for analyses where including the various size scales of the molecular clouds is useful, such as size–line width plots. “Leaves” are the smallest of the dendrogram structures, having no substructure of their own. Leaves are bounded by structures called “branches” and “trunks,” the latter of which are the largest and are not bounded by any further structures. However, because of this hierarchical nature, dendrograms count emission multiple times, and so cannot be used in any sort of counting statistic, such as when examining distributions of properties in a histogram. In these cases, we use clumps instead, which have no overlap and so do not multiply count emission. We use dendrogram structures in Sections 4 and 5 and clumps in Section 6.

2.2. Region Selection

In this work, we are interested in how the properties of the two galaxies vary by region within the galaxies. To define these regions, we use contours of the red filter from Digitized Sky Survey (DSS) images of the two galaxies, which trace the bulk of the stellar population. These contours and the defined regions are shown in Figure 2.

For NGC 1313, we define regions for the bar, the northern arm, and the southern arm, and any structures that fall outside of those regions are considered interarm regions (Figure 2). The bar region is based on the 75% brightness contour in the DSS2-red image, while the arm regions enclose the emission within the 60% contours, then follow the arm pattern out to the edges of the CO(2–1) map following the 40% contour. We separately consider the northern and southern arms.

Since NGC 7793 is a flocculent spiral and does not have clearly defined arms, we instead split the galaxy up into a circular “center” region that follows the 75% brightness contour in the DSS2-red image, and a “ring” region surrounding the center following the 60% contour (Figure 2). The rest of the structures are considered part of the “outer” region.

3. Cluster Catalogs

As in Paper I, we use the catalogs of identified star clusters and their spectral energy distribution fitted masses, ages, and extinctions from the LEGUS collaboration, which are based on the methodology of Adamo et al. (2017). For NGC 1313 and NGC 7793, we expect the 90% mass completeness limit of these catalogs to be approximately $1000 M_{\odot}$ for clusters with ages of up to 200 Myr. Further details about the cluster catalogs used in this study can be found in Paper I.

In Table 2, we report the number of clusters in each galaxy as well as in each of the subgalactic regions. Also shown is the number of clusters that are massive ($>10^4 M_{\odot}$), young (<10 Myr), or both. We also report in this table the number of molecular gas structures, and how many clumps are massive

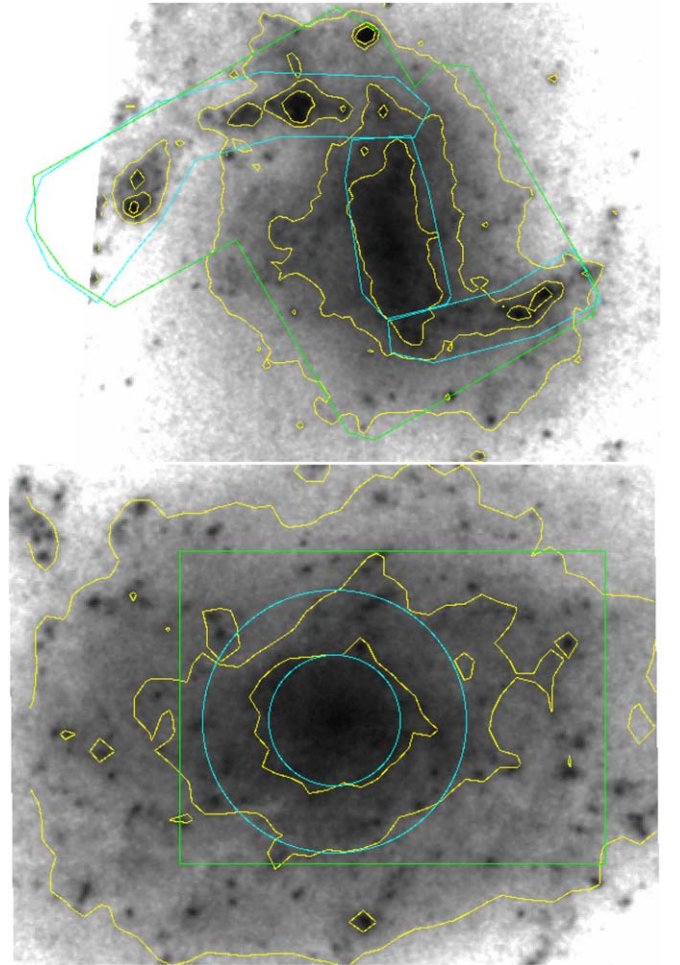


Figure 2. DSS2-red images of NGC 1313 (top) and NGC 7793 (bottom) in gray scale, with yellow contours tracing 40%, 60%, and 75% of the maximum brightness in each image. The green outlines show the observational footprints of the ALMA CO(2–1) maps, and the defined regions are shown in cyan. In NGC 1313, these regions are the northern arm, bar, and southern arm, and in NGC 7793 they are the “center” and “ring” regions. The clouds that are not inside any of the regions are defined to belong to the interarm region of NGC 1313 and to the outer region of NGC 7793.

($>10^4 M_{\odot}$). This table is adapted from Table 3 in Paper I, which gave these numbers for the galaxies as a whole.

From Table 2 we see that the molecular clouds and star clusters in NGC 7793 are fairly evenly distributed (since the areas of the center, ring, and outer regions are consecutively larger), with only the exception of a slight excess of massive gas clumps in the ring region. In NGC 1313, the molecular clouds are much more abundant in the arms than in the bar or interarm regions, but there are more clusters in the bar and interarm regions than in the arms, especially massive ones. However, the region with the most young clusters and young massive clusters is the northern arm. A similar excess is not seen in the southern arm. This is surprising since we expect the two spiral arms to behave in similar ways, though perhaps not so surprising given that the southern arm is closer to the site of a burst in star formation (Larsen et al. 2007; Silva-Villa & Larsen 2012).

3.1. Cluster Property Distributions

To further examine how the cluster populations in each subgalactic region compare, we plot their mass and age

Table 2
Number of Cloud Structures and Clusters in Each Galaxy and Region

Galaxy	Region	Molecular Gas Structures					LEGUS Clusters			
		Trunks	Branches	Leaves	Clumps	Massive Clumps ^a	All	Young ^b	Massive ^a	YMCs ^{a,b}
NGC 1313	All	65	82	442	531	137	1201	618	333	37
	Bar	7	1	61	69	7	380	184	107	8
	N Arm	20	32	161	193	62	297	243	48	18
	S Arm	27	44	156	188	55	145	93	32	7
	Interarm	11	5	64	82	13	379	98	146	4
NGC 7793	All	130	187	761	965	306	467	296	53	3
	Center	22	63	162	203	81	57	22	7	0
	Ring	46	63	277	354	118	108	38	15	2
	Outer	62	61	322	408	107	302	109	31	1

Notes.

^a The threshold used to define “massive” for both clumps and clusters in this table is $M > 10^4 M_{\odot}$.

^b The threshold used to define “young” for clusters is age < 10 Myr.

distributions using Gaussian kernel density estimations (KDEs) from `scipy` (Virtanen et al. 2020), and cumulative distribution functions (CDFs). We use both of these depictions since KDEs are more intuitive to interpret, but are subject to binning effects, while CDFs do not rely on binning and so are more robust but less intuitive in understanding the underlying distribution. For figure clarity, we show only the KDEs and not the underlying histograms. For the KDEs in this section and in Section 6, we adopt a scalar estimator bandwidth of 0.5 dex to make comparisons between regions and properties as direct as possible. These distributions are shown in Figures 3 and 4, and include mass distributions for both the full cluster population and only the young (< 10 Myr) clusters.

In NGC 1313, there are clear, distinct differences in the mass and age distributions of the full cluster populations in these regions. The northern arm has much lower cluster masses than the other regions, but also is most heavily skewed toward young clusters. Meanwhile, the interarm region is more dominated by high-mass, older clusters. The southern arm and the bar have a fairly similar mass distribution, though the bar tends to have older clusters than the southern arm. When considering only young clusters, the differences in mass distribution between regions are much smaller by eye, to the point of appearing negligible.

In NGC 7793, the center region has a bump at high masses ($\sim 10^{6.5} M_{\odot}$), but the CDF appears to show that all three regions have nearly identical mass distributions. These two supermassive clusters in the center of NGC 7793 are relatively old, with fitted ages of 0.9 and 12 Gyr. We consequently deem them largely irrelevant to the current study and will disregard them for the remainder of this work. When considering only the young clusters, the center region instead has the steepest mass distribution, while the outer region has the most clusters at high masses. The age distributions between the regions are also quite similar. Overall, this suggests that the properties of the cluster population in NGC 7793 are fairly uniform throughout the galaxy.

4. Size–Line Width Relation

To compare the molecular cloud properties in the regions of these two galaxies, we first look at their size–line width relation (Larson 1981). We fit power laws to the dendrogram structures

in each region of the form

$$\sigma_v = a_0 R^{a_1}. \quad (1)$$

The fitted slope (a_1) of this relation has been measured in many environments and can vary largely based on the resolution, the molecular tracer, or the methods used to measure sizes and line widths (e.g., Solomon et al. 1987; Bolatto et al. 2008; Wong et al. 2011, 2022; Faesi et al. 2016; Nayak et al. 2016; Rice et al. 2016; Miville-Deschênes et al. 2017; Indebetouw et al. 2020; Finn et al. 2022). These slopes are also often poorly constrained and difficult to compare. We therefore focus primarily only on comparisons between regions in this study, and we fit only the intercept of this power-law relation, holding the slope constant at a value of $a_1 = 0.5$. This fitted intercept indicates the relative amount of kinetic energy in clouds of a given size scale between regions. The assumed value of the fixed slope affects the value of the fitted intercept, but not conclusions about the relative kinetic energy in the regions.

In Paper I, we fit intercepts of $a_0 = 0.41 \pm 0.01$ for NGC 1313, and $a_0 = 0.33 \pm 0.01$ for NGC 7793, indicating that the molecular clouds in NGC 1313 have significantly higher kinetic energies than those in NGC 7793. The size–line width relations for each of the regions in the two galaxies are shown in Figure 5 and the fitted values for each region and the galaxies as a whole are reported in Table 3.

The regions of NGC 1313 show a spread of kinetic energies, with the southern arm having the highest intercept, followed by the northern arm, the bar, then the interarm regions. The fitted intercept for the southern arm is significantly higher than the intercepts for the bar and the interarm region, though it is just barely consistent within 3σ with that for the northern arm. Similarly, the northern arm’s intercept is significantly higher than the interarm region’s but consistent within 3σ with the bar’s. The bar and interarm regions are consistent with each other as well. These fitted intercepts suggest that the gas in the spiral arms of NGC 1313 has higher kinetic energy than the gas in the bar and interarm regions.

In NGC 7793, the intercepts have a much smaller range than those in NGC 1313, and all are consistent with each other within 3σ . The center of NGC 7793 is most similar in intercept to the northern arm of NGC 1313, while the outer region is most similar to the bar.

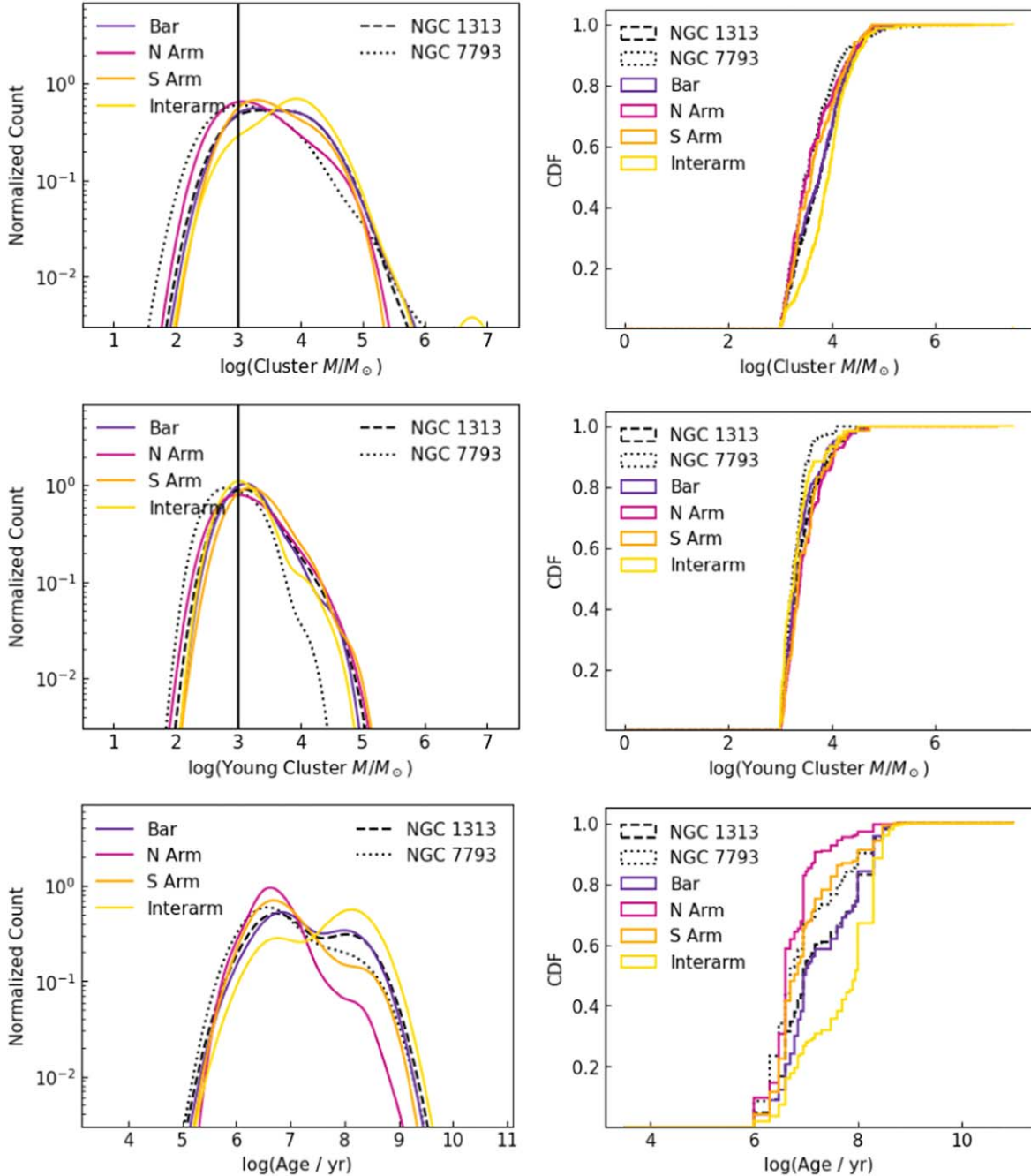


Figure 3. Distributions of the cluster parameters for the bar, northern arm, southern arm, and interarm regions of NGC 1313 using KDEs (left) and CDFs (right). The global property distributions of clusters in NGC 1313 and NGC 7793 are also shown as black dashed and dotted lines, respectively, and are the same as those in Figure 3 of Paper I. We show mass distributions for both the full cluster population (top) and only the young (<10 Myr) clusters (middle). The estimated mass completeness limit of $1000 M_{\odot}$ is shown as a vertical line in the top two left panels, and the CDFs of the mass distributions only include clusters above this mass limit. The age distributions do not include clusters that are likely to have incorrect ages due to the age/reddening degeneracy (Whitmore et al. 2023).

5. Virialization

We next compare the balance between gravitational and kinetic energy in the clouds of the different regions by plotting their velocity metrics, σ_v^2/R , against their surface densities, Σ (Figure 6). The line of virial equilibrium is shown as a dashed line, where gravity is balanced by kinetic energy. Above this line, clouds would be supervirial and dominated by kinetic energy, and below this line clouds are subvirial and likely to collapse due to gravity dominating. Clouds can appear supervirial for many reasons, including the possibility that

they are unbound and will disperse, that they are bounded by an external pressure, or that they are in freefall, in which case they would fall along the dotted freefall line, where $\alpha_{\text{vir}} = 2$. In Figure 6, the distribution of clouds in each region is depicted with contours of the two-dimensional KDEs showing 20% and 50% of the maximum density.

In NGC 1313, all of the regions show a dip toward the virial equilibrium line, though the biggest populations close to virial equilibrium are in the bar and the interarm regions, where the 50% density contours also show that dip. The southern arm appears to extend higher in the plot, suggesting that more of its clouds are

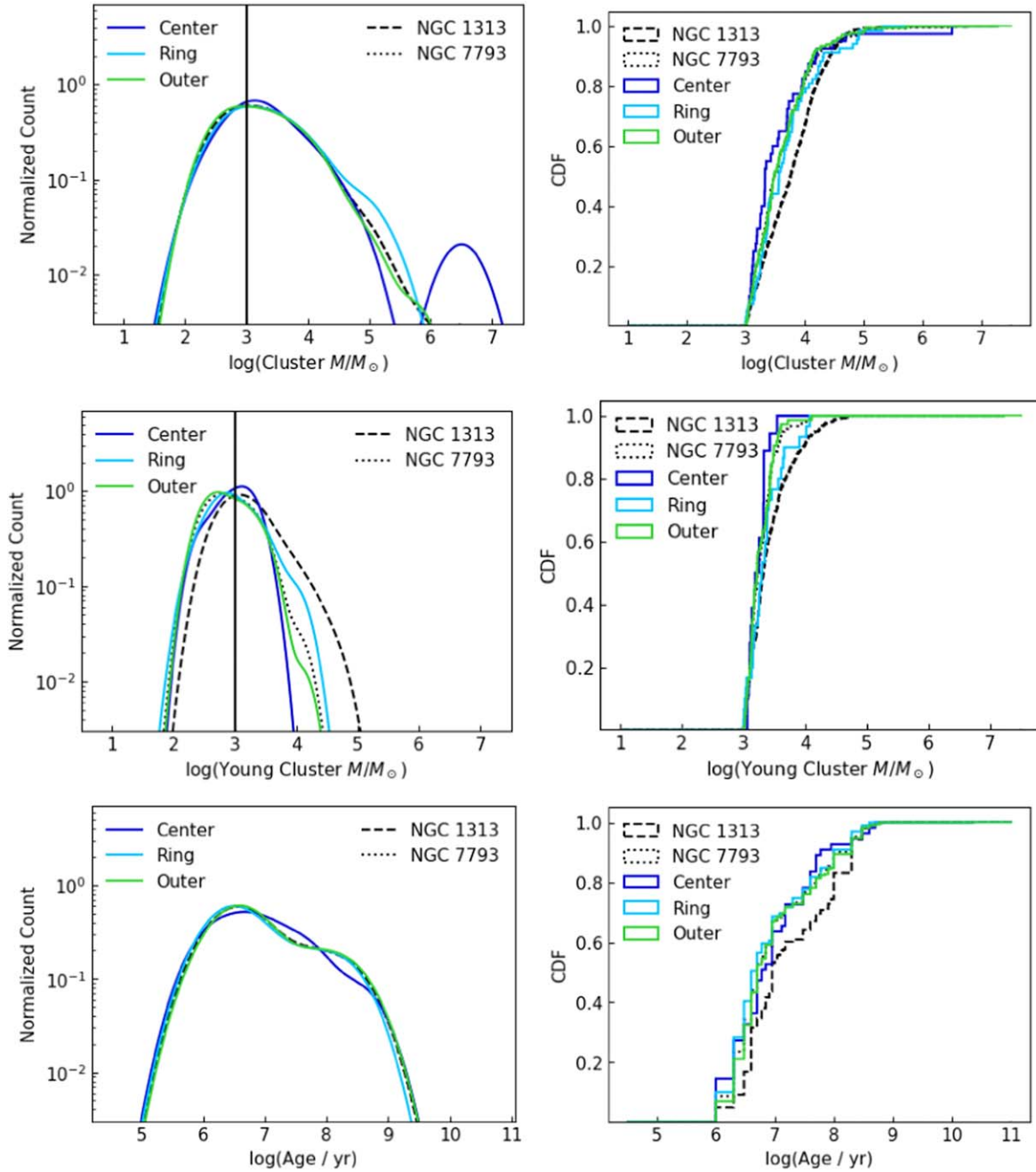


Figure 4. Distributions of the cluster parameters for the center, ring, and outer regions of NGC 7793 using KDEs (left) and CDFs (right). The global property distributions of clusters in NGC 1313 and NGC 7793 are also shown as black dashed and dotted lines, respectively, and are the same as those in Figure 3 of Paper I. We show mass distributions for both the full cluster population (top) and only the young (<10 Myr) clusters (middle). The estimated mass completeness limit of $1000 M_{\odot}$ is shown as a vertical line in the top two left panels, and the CDF of the mass distribution only includes clusters above this mass limit. The age distributions do not include clusters that are likely to have incorrect ages due to the age/reddening degeneracy (Whitmore et al. 2023).

either unbound or would require an external pressure to remain bound compared to the other regions. It seems likely that this is related to the interaction history of NGC 1313 in the southwest since simulations show interaction causing clouds to become unbound (Nguyen et al. 2018; Pettitt et al. 2018). Interestingly, the bar of NGC 1313 does not have more clouds in the unbound or pressure-bound region of the plot than in other regions despite containing the galactic center of NGC 1313 and despite the fact that many other galactic centers exhibit high external pressures (Donovan Meyer et al. 2013; Colombo et al. 2014; Kauffmann et al. 2017; Sun et al. 2018; Walker et al. 2018). This is especially pronounced in the findings of Sun et al. (2020) that velocity

dispersions and external pressures are most enhanced in the centers of barred galaxies.

In NGC 7793, the three regions once again appear more uniform than those in NGC 1313, although the center region does extend higher in the plots, suggesting that it has more clouds that are unbound or require external pressure than the ring and outer regions as we would expect for a galactic center. The ring and outer regions appear very similar, suggesting there is little variation in the virialization of clouds outside of the galaxy center. None of the regions of NGC 7793 however show a dip toward virial equilibrium like that seen in every region of NGC 1313, other than the slight dip in the outer region.

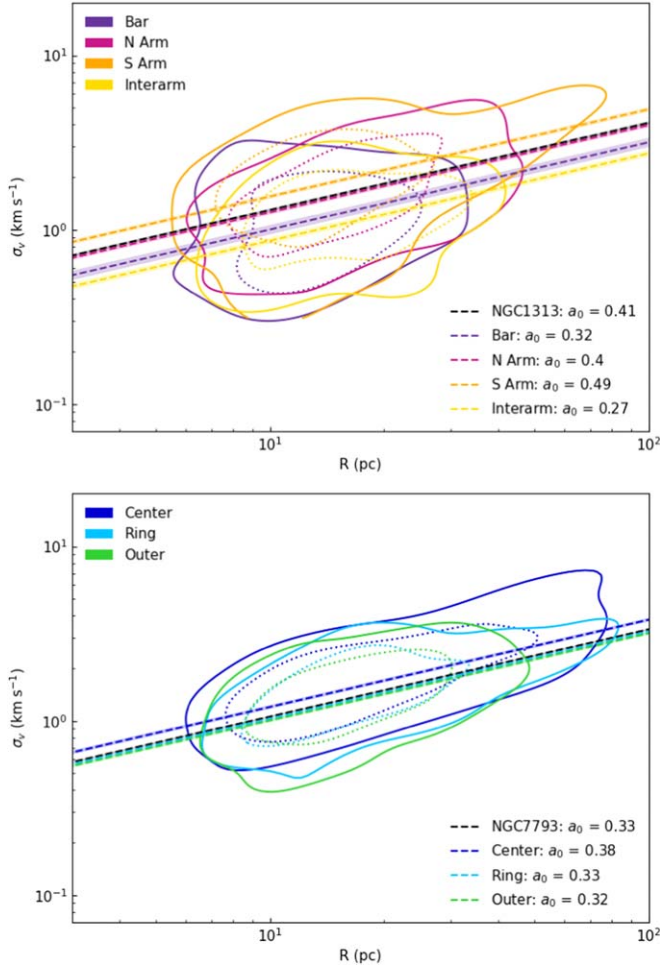


Figure 5. Deconvolved velocity dispersions plotted against deconvolved radii of dendrogram structures in different regions of NGC 1313 (top) and NGC 7793 (bottom) showing the 20% KDE contours as solid lines and the 50% contours as dotted lines. The plots show the fitted power laws with the slope held constant at $a_1 = 0.5$ with the resulting intercepts shown in the lower right corners. Their respective 1σ errors are shown as shaded regions.

Table 3

Fitted Intercepts for Size–Line Width Relation with Fixed Slope of $a_1 = 0.5$

Galaxy	Region	Intercept, a_0
NGC 1313	Global	0.41 ± 0.01
	Bar	0.32 ± 0.02
	N Arm	0.40 ± 0.01
	S Arm	0.49 ± 0.02
	Interarm	0.27 ± 0.01
NGC 7793	Global	0.33 ± 0.01
	Center	0.38 ± 0.01
	Ring	0.33 ± 0.01
	Outer	0.32 ± 0.01

Note. Global fitted intercepts from Paper I.

6. Property Distribution Comparisons

6.1. NGC 1313 Region Comparisons

We next compare the distributions of cloud properties within the bar, northern arm, southern arm, and interarm regions of NGC 1313 by looking at the KDEs and CDFs of the nonoverlapping clump structures. The distributions of the

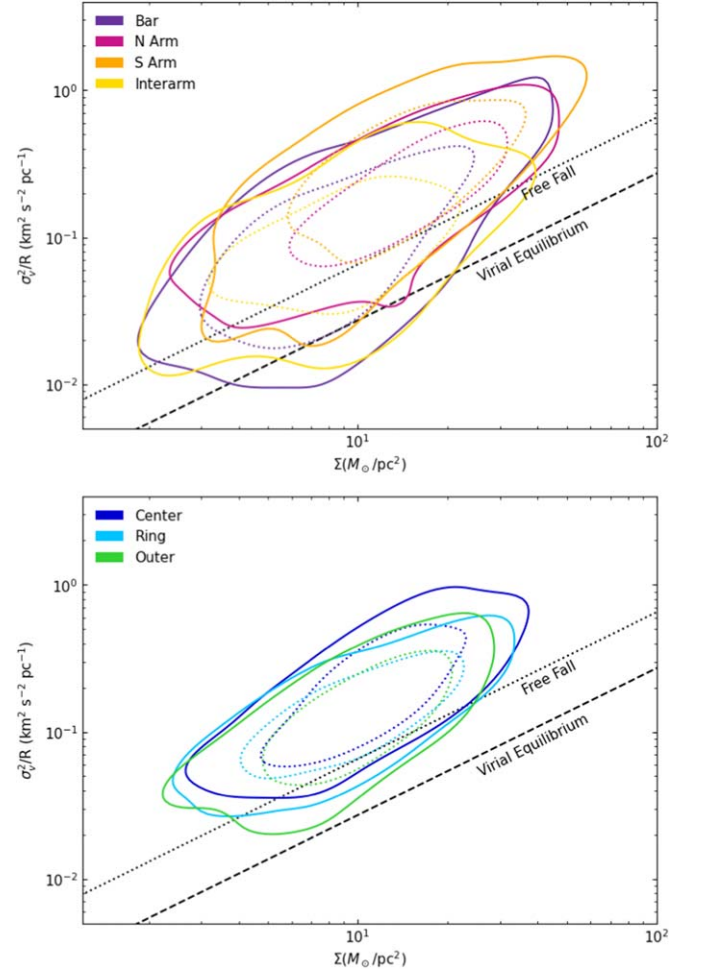


Figure 6. The velocity metric plotted against the surface density of the dendrogram structures in the different regions of NGC 1313 (top) and NGC 7793 (bottom) showing the 20% KDE contours as solid lines and the 50% contours as dotted lines. The dashed line shows where clouds in virial equilibrium would fall, the area above the line being dominated by kinetic energy. Clouds that have begun freefall collapse would also have enhanced kinetic energy and fall along the dotted line.

global NGC 1313 and NGC 7793 cloud populations from Paper I are shown as well for comparison. The observed mass, radius, and line width distributions are shown in Figure 7, and the properties derived from them are shown in Figure 8. For figure clarity, we show only the KDEs and not the underlying histograms.

There is a large difference in the mass distributions, with the spiral arms having significantly more massive clouds than the bar or interarm regions. The northern arm also appears to have slightly higher masses than the southern arm. These regional mass distribution differences agree with previous results that clouds in spiral arms truncate at higher masses than clouds in interarm regions, seen in both observations (Koda et al. 2009; Colombo et al. 2014; Rosolowsky et al. 2021) and simulations (Nguyen et al. 2018; Pettitt et al. 2018; Dobbs et al. 2019). The differences between cloud size distributions are minimal, though the bar region appears to have slightly fewer clouds with large radii. The spiral arms have similar line width distributions and are higher than the other two regions, where the interarm region has the smallest line widths, again matching previous results (Colombo et al. 2014; Sun et al. 2020; Rosolowsky et al. 2021; Koda et al. 2023).

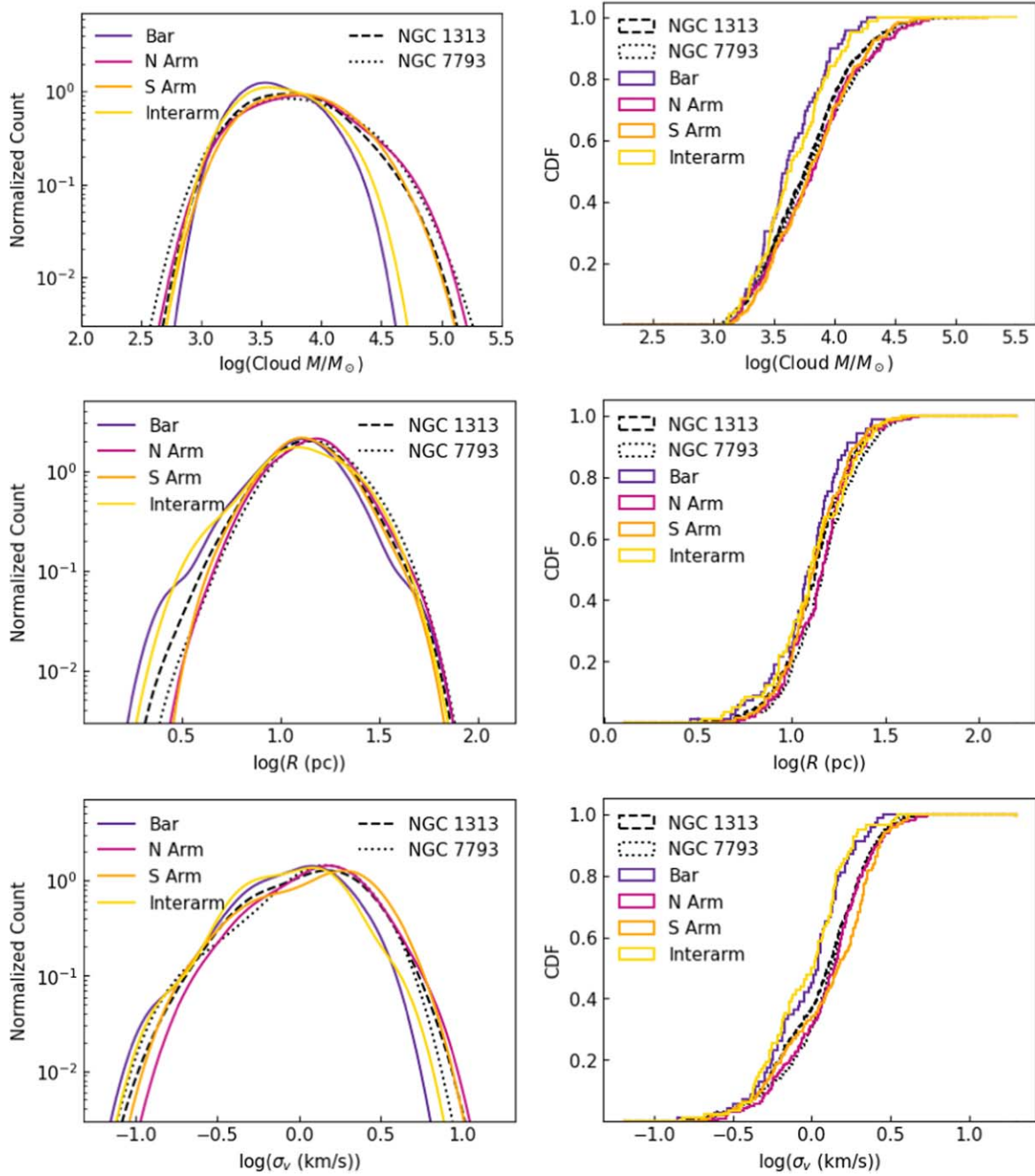


Figure 7. Distributions of the observed parameters for the bar, northern arm, southern arm, and interarm regions of NGC 1313 using KDEs (left) and CDFs (right). Also shown are the global distributions for each galaxy from Paper I.

Despite the large difference in mass distributions, the properties derived from the mass, radius, and line width do not show strong distinctions between regions. Most notably, the interarm and bar regions appear to have the lowest virial parameters, surface densities, and external pressures. The southern arm also appears to have slightly higher surface densities and pressures compared to the northern arm and other regions.

It is particularly surprising that we see so little difference in surface densities between the arm and interarm regions, since a notable difference has often been observed in other studies (Colombo et al. 2014; Sun et al. 2020; Rosolowsky et al. 2021; Koda et al. 2023). We also note that the clouds in the bar of

NGC 1313 mostly have less extreme properties than those in the arms, whereas other studies have often seen enhancements of the velocity dispersion, surface density, and pressure in bars and galactic centers (Sun et al. 2020; Rosolowsky et al. 2021; Ali et al. 2023). This may not be so surprising since Querejeta et al. (2021) have reported large variations in the properties of molecular gas in bars, potentially because star formation in bars is episodic.

As in Paper I, we quantify these differences in property distributions using bootstrapped two-sample Kolmogorov–Smirnov (KS) tests and Anderson–Darling (AD) tests. Using the full sample size of the galaxies results in an overpowered statistic as described in Lazariv & Lehmann (2018), where the

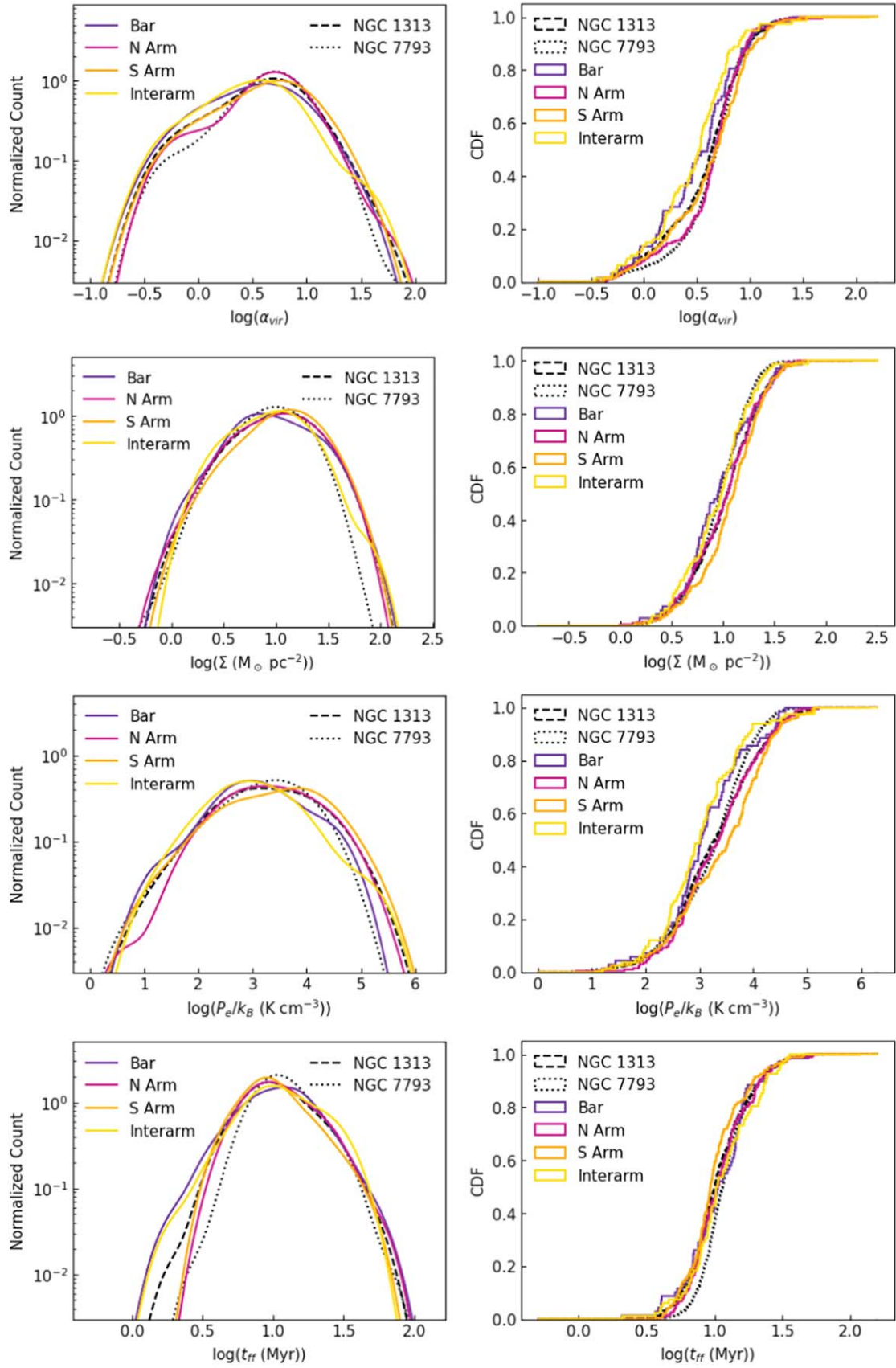


Figure 8. Distributions of the derived parameters for the bar, northern arm, southern arm, and interarm regions of NGC 1313 using KDEs (left) and CDFs (right). Also shown are the global distributions for each galaxy from Paper I.

tests detected every small variation in the distribution, even those that were well below the measurement errors. Since these overpowered tests are unreliable, we instead perform a bootstrapped version, taking 1000 random subsamples and reporting the average p -value of the tests performed on the subsamples. We choose a sample size of 65 because we are limited by the number of clumps identified in the bar of NGC 1313. We perform these bootstrapped tests for every property and for every combination of subgalactic regions in both galaxies and plot the results in the [Appendix](#).

Looking at the bootstrapped KS and AD tests for pairings of the regions in NGC 1313, we find that none of the derived properties have statistically significant differences ($p < 0.05$) in their distributions between regions except for the southern arm having significantly higher pressure than the bar and interarm regions. There are, however, statistically significant differences in their mass and line width distributions. The absolute values of these test results are highly subject to the size of the subsamples used in the bootstrapping, and so we do not take these as indications of whether the distributions are actually different, but rather as an indication that some properties are more likely to be different than others.

6.2. NGC 7793 Region Comparisons

We next examine the distribution of cloud properties within the center, ring, and outer regions of NGC 7793. The observed mass, radius, and line width distributions are shown in Figure 9, and the properties derived from them are shown in Figure 10.

The distributions in NGC 7793 vary from the center of the galaxy to the outer region, with the center having more extreme properties, such as higher masses, larger line widths, higher virial parameters, and higher external pressures. This generally matches what was found in other surveys for the centers of galaxies (Donovan Meyer et al. 2013; Colombo et al. 2014; Sun et al. 2020; Koda et al. 2023). There is not as much difference, however, in the distribution of radii, surface densities, or freefall times. In most cases, the ring and outer regions have very similar distributions, while the center deviates more.

These similarities and differences appear as well in comparisons of the bootstrapped KS and AD tests shown in the [Appendix](#). None of the cloud or cluster properties, either observed or derived, have statistically significant differences ($p < 0.05$) in their distributions among the regions of NGC 7793 for both the KS and AD tests. The only exception is the center region having significantly greater line widths than the outer region based on the AD test. Again, the absolute values of these test results are highly subject to the size of the subsamples used in the bootstrapping, so we do not take these results to indicate whether the distributions are actually different, but rather that some properties are more likely to be different than others.

6.3. Intergalaxy Region Comparisons

Based on the regional distributions of NGC 1313 shown in Figures 7 and 8, none of the regions of NGC 1313 have similar property distributions to the global distributions of NGC 7793 clouds across all properties. The northern arm has the most similar mass distribution and α_{vir} distribution to NGC 7793, but the interarm region has the most similar surface density

distribution, and in other property distributions, such as the external pressure and freefall time distributions, no NGC 1313 region is similar to the clouds in NGC 7793. This suggests that the environment of a flocculent spiral like NGC 7793 is quite different from both clearly defined arms and their interarm regions. Most notably, every region of NGC 1313 contains, on average, clouds with higher surface densities and shorter freefall times than NGC 7793.

This difference between the galaxies' regions is seen again in Figures 9 and 10, which show that none of the regions of NGC 7793 have similar virial parameters, surface densities, external pressures, or freefall times to the global distributions of NGC 1313. The ring region of NGC 7793 appears to have the most similar mass, radius, and line width distributions to the global distribution of NGC 1313.

Considering the comparisons of the bootstrapped KS and AD tests in the [Appendix](#), some of the most significant differences among all the pairings for both tests are between the central region of NGC 7793 and the bar and interarm regions of NGC 1313, for almost every property, with the notable exception of surface density and freefall time. This is somewhat surprising since the bar of NGC 1313 encompasses that galaxy's own central region and galaxy centers usually have more extreme cloud properties (Donovan Meyer et al. 2013; Colombo et al. 2014; Sun et al. 2020; Ali et al. 2023; Koda et al. 2023). One other notable difference from the KS and AD tests is that the southern arm of NGC 1313 has statistically significant shorter freefall times than all regions of NGC 7793. This is not true for the northern arm. Since the absolute values of the resulting p -values of these bootstrapped tests are so easily influenced by subsample size, we do not take these results to indicate whether the distributions are actually statistically different, but rather to indicate which property distributions are most likely to be different.

7. Discussion

In Table 4, we briefly outline the differences in each property between the two galaxies as discussed in Paper I and among the regions within each galaxy. There does not appear to be any singular property that has an overwhelming influence on the star formation of either the galaxy or the galactic regions.

While the differences in cloud properties between the two galaxies as seen in Paper I are surprisingly small, there is considerable variation between regions within each galaxy, especially within NGC 1313. This suggests that the local environment has a much stronger influence on cloud properties than the global galaxy environment. This was also seen when comparing regional variations and galaxy-to-galaxy variations in the PHANGS sample at 100 pc resolution (Sun et al. 2022).

Comparing the regional variations within the two galaxies, NGC 7793 appears much more uniform across the galaxy than NGC 1313, with more extreme properties only being seen in the center of the galaxy. The lack of clearly defined arm and interarm regions makes direct comparison tricky, but it is at least clear that no region of NGC 7793 contains clouds with surface densities, pressures, or line widths as high as the most extreme properties found in the arms of NGC 1313 (Figures 9 and 10). Elmegreen (2009) posits that the degree of dispersion of the density probability distribution function determines the ability of a region to form massive, gravitationally bound star clusters. Regions that have a larger spread in densities will also achieve higher densities, and so be able to form massive

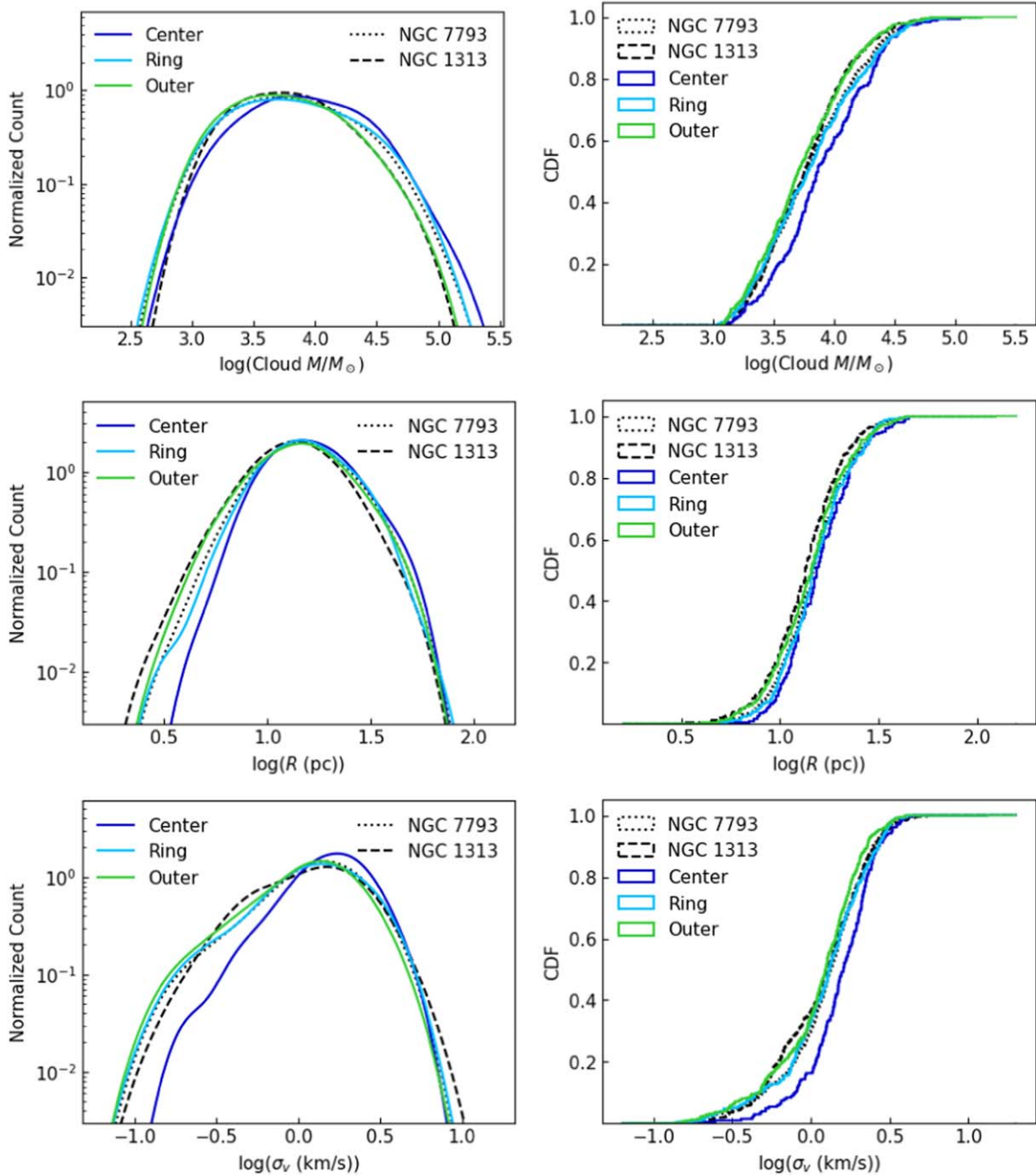


Figure 9. Distributions of the observed parameters for the center, ring, and outer regions of NGC 7793 using KDEs (left) and CDFs (right). Also shown are the global distributions for each galaxy from Paper I.

clusters. It would follow then that NGC 1313 is able to create more massive star clusters than NGC 7793 because it has a greater variety of subgalactic environments, including strong spiral arm environments that have higher pressures and densities. The lack of similarly large differences in the mass distributions of young clusters could be due to the fact that the clusters in the LEGUS catalogs do not include many of the youngest, highly embedded clusters (Messa et al. 2021), and they are no longer closely associated with their natal molecular gas, as seen in Paper I.

It is interesting to note as well that the southern arm of NGC 1313 has slightly more extreme properties than its northern arm. We know from measurements of HI and the star formation history of NGC 1313 (Peters et al. 1994; Larsen

et al. 2007; Silva-Villa & Larsen 2012; Hernandez et al. 2022) that it is experiencing an interaction, which likely caused a recent burst in star formation in the southwest of the galaxy approximately 100 Myr ago. This interaction may also be influencing the difference in cloud properties between the northern and southern arms, suggesting that satellite galaxy interaction can drive variations in local cloud properties.

Meanwhile in NGC 7793, the loose, poorly defined spiral arms do not result in the majority of the clouds mimicking either the arm or the interarm regions of NGC 1313. Rather, the clouds throughout the galaxy have similar masses and kinetic energies to the arms of NGC 1313, but their surface densities and pressures are more similar throughout to those of the bar and interarm regions of NGC 1313. These differences overall

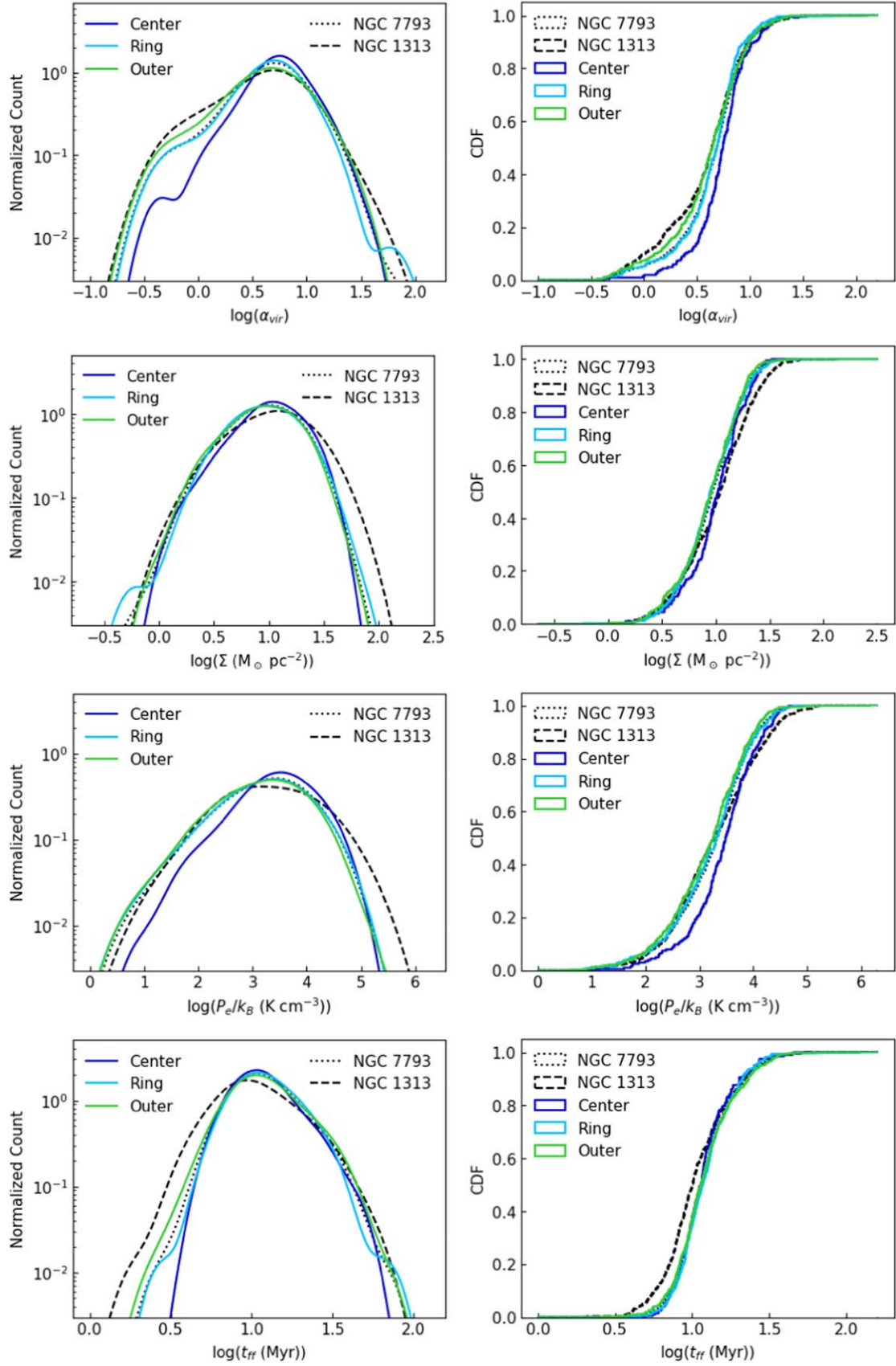


Figure 10. Distributions of the derived parameters for the center, ring, and outer regions of NGC 7793 using KDEs (left) and CDFs (right). Also shown are the global distributions for each galaxy from Paper I.

Table 4
Comparison of Observed Properties between Environments

Property	Global Difference	NGC 1313 Regional	NGC 7793 Regional
Cluster mass distribution	NGC 1313 more massive	Interarm most massive, N arm least	No difference
Young cluster mass distribution	NGC 1313 more massive	No difference	Outer most massive
Cluster age distribution	NGC 1313 older	Interarm oldest, N arm youngest	No difference
Size–line width intercept	No difference	S arm highest, interarm lowest	Center highest
Virialization plot	NGC 1313 closer to virial	Bar and interarm closest to virial	Center furthest from virial
Cloud mass distribution	No difference	Arms most massive	Center most massive
Radius distribution	NGC 7793 larger	No difference	No difference
Line width distribution	No difference	Arms largest	Center largest
Virial parameter distribution	NGC 1313 lower	Interarm lowest	Center highest
Surface density distribution	NGC 1313 higher	S arm highest, interarm lowest	No difference
External pressure distribution	NGC 1313 higher	S arm highest, interarm lowest	Center highest
Freefall time distribution	NGC 1313 shorter	No difference	No difference

result in higher virial parameters and longer freefall times throughout NGC 7793 than in any region in NGC 1313. Essentially, NGC 7793 has clouds that are just as massive and have just as much kinetic energy as those of NGC 1313, but they are puffier and less pressurized, and so are less inclined to collapse and form stars. This mirrors the findings in Paper I that the consumption time of the molecular mass in NGC 7793 is much longer than that in NGC 1313. Strong spiral density waves are likely to perturb molecular clouds to induce collapse while they are in the arms, and then shear the clouds into more diffuse gas as they enter the interarm regions. The lack of strong spiral density waves in NGC 7793 allows the clouds to exist for a longer time in a dormant state where they are neither collapsing nor being torn apart.

A notable exception to the uniformity of NGC 7793 is the center of the galaxy, where the clouds have higher masses, and fewer clouds have low line widths, virial parameters, and pressures. This is reminiscent of the center of our own Galaxy, where clouds have more extreme properties and some massive star clusters are present, but it is still forming fewer stars than expected based on the gas properties (Kauffmann et al. 2017; Walker et al. 2018), though this phenomenon may be partly accounted for by the metallicity dependence of the X_{CO} factor (Evans et al. 2022).

This work represents the highest-resolution direct comparison of the molecular cloud properties in spiral arm, interarm, and flocculent environments to date. Comparing our results at 13 pc to other results at ~ 40 –100 pc resolution reveals further insights about how the molecular gas behaves at different spatial scales. For the most part, we see similar trends in that the spiral arms and galaxy centers have higher masses, line widths, and pressures than the interarm and outer regions of the galaxies. However, we see notably less difference in the surface densities between these regions than other studies have found at lower resolution (Colombo et al. 2014; Sun et al. 2020; Rosolowsky et al. 2021; Koda et al. 2023). This could indicate that at lower resolution, the sparse clouds of the interarm and outer regions are spread out to lower apparent surface density by the large beam size. In the arm and central regions, the clouds are sufficiently clustered that the beam is filled by clouds getting blended together, and so the apparent surface density remains high. If this is the case, the surface density seen by lower-resolution studies could be indicative of the sparsity of molecular clouds rather than their true surface density.

8. Conclusions

We present a comparison of the molecular gas properties in different regions of two galaxies, barred spiral NGC 1313, which is forming many massive clusters, and flocculent spiral NGC 7793, which is forming significantly fewer massive clusters despite having a similar SFR. Using the cloud properties calculated in Paper I, we split the galaxies into regions including the bar, northern arm, southern arm, and interarm regions of NGC 1313 and center, ring, and outer regions of NGC 7793 (since the latter has no clearly defined spiral arms for us to use). We examine how the molecular cloud properties vary by region in these two galaxies and how those regions and their differences compare between the two galaxies. Our major results are summarized below.

1. The properties of the cluster population vary slightly by region, with the interarm region of NGC 1313 having the oldest and most massive clusters, and the northern arm having the youngest and least massive clusters. By number, the southern arm has significantly fewer young, massive clusters than the northern arm. The clusters in NGC 7793 show relatively little variation with the region of the galaxy. However, when only young clusters are considered, the center region of the galaxy has the fewest massive clusters.
2. We fit power laws to the size–line width relation for the regions of the two galaxies, holding the slope fixed at a value of $a_1 = 0.5$ to determine relative kinetic energies from the fitted intercepts. The spiral arms of NGC 1313 have higher fitted intercepts, and so more kinetic energy, than the bar or interarm regions. The fitted intercepts of the regions in NGC 7793 meanwhile do not differ by more than 3σ .
3. NGC 1313 has more clouds near virial equilibrium than NGC 7793 for all regions in NGC 1313 and all regions of NGC 7793. The southern arm of NGC 1313 and the center region of NGC 7793 both show a greater spread toward the unbound region of parameter space, suggesting that more of their clouds are either unbound or would require an external pressure to remain bound.
4. The spiral arms of NGC 1313 tend to have more extreme cloud properties (higher masses, line widths, surface densities, pressures, and virial parameters) than the bar or interarm regions, and they also host significantly more of the molecular gas mass. In some properties, such as line width, surface density, and pressure, the southern arm

appears more extreme than the northern arm. This could be because the southern arm is more strongly influenced by the galaxy interaction to the southwest. The greater number of star clusters and the greater masses of those star clusters in NGC 1313 may be driven by its greater variation in environment and cloud properties. Its greater variation may allow for more extreme cloud properties to arise and so drive more intensive star formation.

5. The center region of NGC 7793 has more extreme properties than the ring and outer regions, which are quite similar to each other. This suggests that the disk of NGC 7793 has relatively uniform cloud properties, which is consistent with the finding of less variation in cluster properties among the regions there than in NGC 1313. The cloud properties in NGC 7793 are not particularly similar to those of any one region of NGC 1313, suggesting that flocculent environments are distinct from either strong spiral arms or their interarm regions. NGC 7793 has clouds that are as massive and have as much kinetic energy as those of NGC 1313, but have slightly larger radii and are less dense and pressurized, and so are less inclined to collapse and form stars. This indicates that in NGC 7793, clouds are likely to be dormant and form few stars for most of their lifetime, while in NGC 1313 clouds are perturbed by spiral density waves and either collapse and form clusters or are sheared into more diffuse material.
6. We see surprisingly little variation in surface density between the arm and interarm regions in NGC 1313 given previous lower-resolution results. This suggests that differences in surface density between arm and interarm regions observed in galaxies at ~ 40 pc or coarser resolution could be driven by variations in the number of clouds filling the beam, rather than by intrinsic variations in the surface densities of the clouds themselves.

Acknowledgments

This material is based on work supported by the National Science Foundation Graduate Research Fellowship Program under grant No. 1842490. Any opinions, findings, and conclusions or recommendations expressed in this material are those of the authors and do not necessarily reflect the views of the National Science Foundation.

K.G. is supported by the Australian Research Council through the Discovery Early Career Researcher Award (DECRA) Fellowship (project No. DE220100766) funded by the Australian government. K.G. is supported by the Australian Research Council Centre of Excellence for All Sky Astrophysics in 3 Dimensions (ASTRO 3D), through project No. CE170100013. M.R.K. acknowledges funding from the Australian Research Council through Laureate Fellowship LF220100020.

This paper makes use of the following ALMA data: ADS/JAO.ALMA#2015.1.00782.S. ALMA is a partnership of ESO (representing its member states), NSF (USA) and NINS

(Japan), together with NRC (Canada), NSC and ASIAA (Taiwan), and KASI (Republic of Korea), in cooperation with the Republic of Chile. The Joint ALMA Observatory is operated by ESO, AUI/NRAO and NAOJ. The National Radio Astronomy Observatory is a facility of the National Science Foundation operated under cooperative agreement by Associated Universities, Inc.

These data are associated with the Hubble Space Telescope (HST) General Observer Program 13364 (PI: D. Calzetti). Support for this program was provided by NASA through grants from the Space Telescope Science Institute. Based on observations obtained with the NASA/ESA HST, at the Space Telescope Science Institute, which is operated by the Association of Universities for Research in Astronomy, Inc., under NASA contract NAS5-26555.

Facility: ALMA, HST (WFC3, ACS).

Software: Pipeline-CASA51-P2-B v.40896 (L. Davis 2024, in preparation), CASA (v.5.1.1-5, v.5.6.1; McMullin et al. 2007), astrodendro (Rosolowsky et al. 2008), quickclump (Sidorin 2017), Astropy (Astropy Collaboration et al. 2013), Matplotlib (Hunter 2007), NumPy (Harris et al. 2020), SciPy (Virtanen et al. 2020).

Appendix KS and AD Tests

As thoroughly discussed in Lazariv & Lehmann (2018), as the sample size increases, the discerning power of KS tests increases. However, KS tests cannot take into account error in the measurements, and so it is possible for a test to become overpowered. Even a small difference in the distribution well below the measurement uncertainty can result in a rejection of the null hypothesis that the distributions are the same. This effect is present in AD tests as well.

To combat overpowered statistical tests, we perform a bootstrapping method to measure the difference in the distributions. We take 1000 random subsamples with a size of 65 data points, perform KS and AD tests between each pairing of regions, and report the average p -value for the 1000 subsamples. We caution that the resulting p -values are highly dependent on the size of the subsample used, and so these results should only be used to compare the differences between properties and regions on equally powered statistical footing. This is meant as an indication of which pairings are the most likely to be different, not of whether the underlying distributions are truly, statistically different. It may be possible to select a subsample size based on the error of the measurements being tested, but that is outside the scope of the current work.

Figure 11 shows the bootstrapped KS statistic for each cloud and cluster property for each pairing of subgalactic region or global distribution for each galaxy. Figure 12 shows the same but for an AD test. KS tests are more influenced by the center of the distribution, while AD tests are more sensitive to the tails.

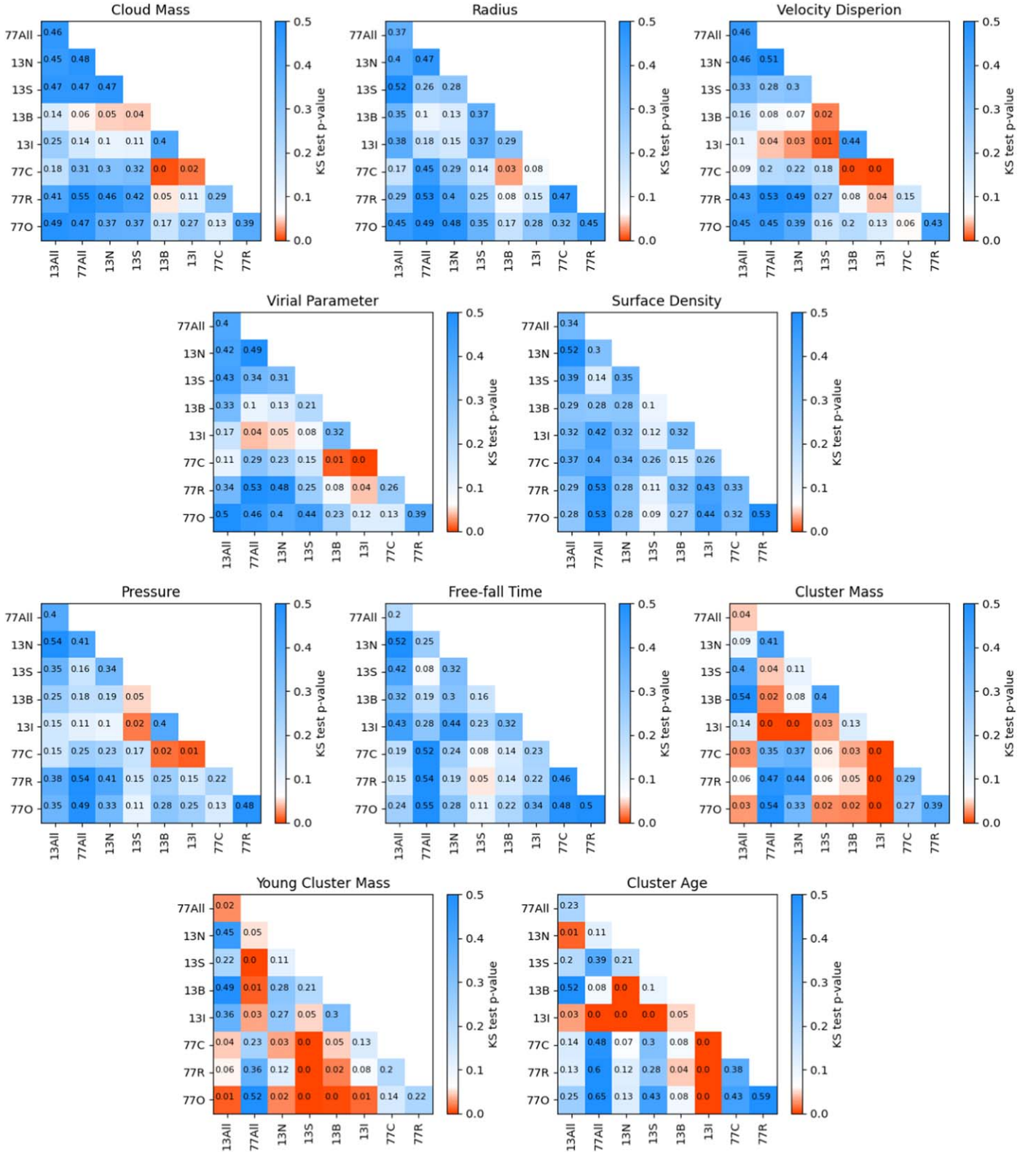


Figure 11. Bootstrapped KS tests for each cloud and cluster property for each pairing of subgalactic region or global distribution for each galaxy. These p -values should be used as an indication of which distributions are the most likely to be different rather than as an absolute metric of whether any one distribution is truly different. Codes for the regions are as follows: “13All” is the global distribution for NGC 1313; “77All” is the global distribution for NGC 7793; “13N,” “13S,” “13B,” and “13I” are the northern arm, southern arm, bar, and interarm regions of NGC 1313; and “77C,” “77R,” and “77O” are the center, ring, and outer regions of NGC 7793.

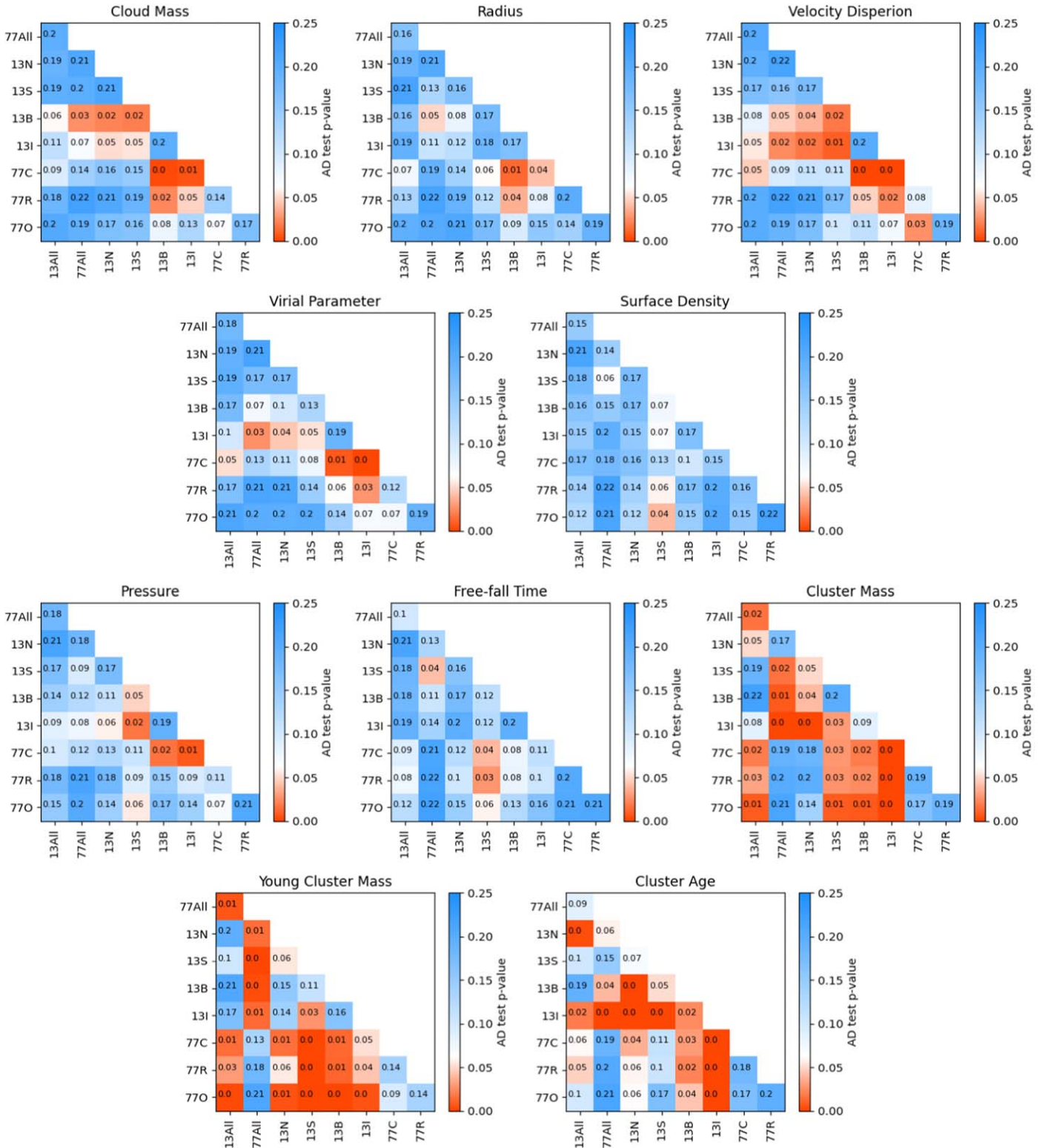





Figure 12. Bootstrapped AD tests for each cloud and cluster property for each pairing of subgalactic region or global distribution for each galaxy. These p -values should be used as an indication of which distributions are the most likely to be different rather than as an absolute metric of whether any one distribution is truly different. Codes for the regions are as follows: “13All” is the global distribution for NGC 1313; “77All” is the global distribution for NGC 7793; “13N,” “13S,” “13B,” and “13I” are the northern arm, southern arm, bar, and interarm regions of NGC 1313; and “77C,” “77R,” and “77O” are the center, ring, and outer regions of NGC 7793.

ORCID iDs

Molly K. Finn <https://orcid.org/0000-0001-9338-2594>
 Kelsey E. Johnson <https://orcid.org/0000-0001-8348-2671>
 Remy Indebetouw <https://orcid.org/0000-0002-4663-6827>

Allison H. Costa <https://orcid.org/0000-0002-7408-7589>
 Angela Adamo <https://orcid.org/0000-0002-8192-8091>
 Alessandra Aloisi <https://orcid.org/0000-0003-4137-882X>
 Lauren Bittle <https://orcid.org/0000-0002-7845-8498>

Daniela Calzetti  <https://orcid.org/0000-0002-5189-8004>
 Daniel A. Dale  <https://orcid.org/0000-0002-5782-9093>
 Clare L. Dobbs  <https://orcid.org/0000-0002-4578-297X>
 Jennifer Donovan Meyer  <https://orcid.org/0000-0002-3106-7676>
 Bruce G. Elmegreen  <https://orcid.org/0000-0002-1723-6330>
 Debra M. Elmegreen  <https://orcid.org/0000-0002-1392-3520>
 Michele Fumagalli  <https://orcid.org/0000-0001-6676-3842>
 J. S. Gallagher  <https://orcid.org/0000-0001-8608-0408>
 Kathryn Grasha  <https://orcid.org/0000-0002-3247-5321>
 Eva K. Grebel  <https://orcid.org/0000-0002-1891-3794>
 Robert C. Kennicutt  <https://orcid.org/0000-0001-5448-1821>
 Mark R. Krumholz  <https://orcid.org/0000-0003-3893-854X>
 Janice C. Lee  <https://orcid.org/0000-0002-2278-9407>
 Matteo Messa  <https://orcid.org/0000-0003-1427-2456>
 Preethi Nair  <https://orcid.org/0000-0001-7069-4026>
 Elena Sabbi  <https://orcid.org/0000-0003-2954-7643>
 Linda J. Smith  <https://orcid.org/0000-0002-0806-168X>
 David A. Thilker  <https://orcid.org/0000-0002-8528-7340>
 Bradley C. Whitmore  <https://orcid.org/0000-0002-3784-7032>
 Aida Wofford  <https://orcid.org/0000-0001-8289-3428>

References

- Adamo, A., Hollyhead, K., Messa, M., et al. 2020, *MNRAS*, **499**, 3267
 Adamo, A., Kruijssen, J. M., Bastian, N., Silva-villa, E., & Ryon, J. 2015, *MNRAS*, **452**, 246
 Adamo, A., Östlin, G., & Zackrisson, E. 2011, *MNRAS*, **417**, 1904
 Adamo, A., Ryon, J. E., Messa, M., et al. 2017, *ApJ*, **841**, 131
 Ali, A. A., Dobbs, C. L., Bending, T. J. R., Buckner, A. S. M., & Pettitt, A. R. 2023, *MNRAS*, **524**, 555
 Astropy Collaboration, Robitaille, T. P., & Tollerud, E. J. 2013, *A&A*, **558**, A33
 Bolatto, A. D., Leroy, A. K., Rosolowsky, E., Walter, F., & Blitz, L. 2008, *ApJ*, **686**, 948
 Brinchmann, J., Charlot, S., White, S. D., et al. 2004, *MNRAS*, **351**, 1151
 Calzetti, D., Lee, J. C., Sabbi, E., et al. 2015, *AJ*, **149**, 51
 Colombo, D., Hughes, A., Schinnerer, E., et al. 2014, *ApJ*, **784**, 3
 Dobbs, C. L., Adamo, A., Few, C. G., et al. 2017, *MNRAS*, **464**, 3580
 Dobbs, C. L., Burkert, A., & Pringle, J. E. 2011, *MNRAS*, **413**, 2935
 Dobbs, C. L., Pettitt, A. R., Corbelli, E., & Pringle, J. E. 2018, *MNRAS*, **478**, 3793
 Dobbs, C. L., & Pringle, J. E. 2013, *MNRAS*, **432**, 653
 Dobbs, C. L., Pringle, J. E., & Naylor, T. 2014, *MNRAS*, **437**, L31
 Dobbs, C. L., Rosolowsky, E., Pettitt, A. R., et al. 2019, *MNRAS*, **485**, 4997
 Donovan Meyer, J., Koda, J., Momose, R., et al. 2013, *ApJ*, **772**, 107
 Elmegreen, B. G. 2009, *Ap&SS*, **324**, 83
 Evans, N. J., Kim, J.-G., & Ostriker, E. C. 2022, *ApJL*, **929**, L18
 Faesi, C. M., Lada, C. J., & Forbrich, J. 2016, *ApJ*, **821**, 125
 Finn, M. K., Indebetouw, R., Johnson, K. E., et al. 2022, *AJ*, **164**, 64
 Finn, M. K., Johnson, K. E., Brogan, C. L., et al. 2019, *ApJ*, **874**, 120
 Finn, M. K., Johnson, K. E., Indebetouw, R., et al. 2024, *ApJ*, **964**, 12
 Gao, Q., Wang, W., Liu, J.-F., & Yoachim, P. 2015, *ApJ*, **799**, 19
 Grasha, K., Calzetti, D., Adamo, A., et al. 2017a, *ApJ*, **840**, 113
 Grasha, K., Calzetti, D., Bittle, L., et al. 2018, *MNRAS*, **481**, 1016
 Grasha, K., Elmegreen, B. G., Calzetti, D., et al. 2017b, *ApJ*, **842**, 25
 Harris, C. R., Millman, K. J., van der Walt, S. J., et al. 2020, *Natur*, **585**, 357
 Hernandez, S., Winch, A., Larsen, S., James, B. L., & Jones, L. 2022, *AJ*, **164**, 89
 Hunter, J. D. 2007, *CSE*, **9**, 90
 Indebetouw, R., Wong, T., Chen, C. H. R., et al. 2020, *ApJ*, **888**, 56
 Johnson, K. E., Leroy, A. K., Indebetouw, R., et al. 2015, *ApJ*, **806**, 35
 Johnson, L. C., Seth, A. C., Dalcanton, J. J., et al. 2016, *ApJ*, **827**, 33
 Johnson, L. C., Seth, A. C., Dalcanton, J. J., et al. 2017, *ApJ*, **839**, 78
 Kauffmann, J., Pillai, T., Zhang, Q., et al. 2017, *A&A*, **603**, A89
 Koda, J., Hirota, A., Egusa, F., et al. 2023, *ApJ*, **949**, 108
 Koda, J., Scoville, N., Sawada, T., et al. 2009, *ApJL*, **700**, 132
 Krahm, G., Finn, M. K., Indebetouw, R., et al. 2024, *ApJ*, in press (arXiv:2401.04835)
 Larsen, S. S., Mora, M. D., Brodie, J. P., & Richtler, T. 2007, in IAU Symp. 241, *Stellar Populations as Building Blocks of Galaxies*, ed. A. Vazdekis & R. Peletier (Cambridge: Cambridge Univ. Press), 435
 Larson, R. B. 1981, *MNRAS*, **194**, 809
 Lazariv, T., & Lehmann, C. 2018, arXiv:1810.09753
 Leroy, A. K., Schinnerer, E., Hughes, A., et al. 2021, *ApJS*, **257**, 43
 McMullin, J. P., Waters, B., Schiebel, D., Young, W., & Golap, K. 2007, in ASP Conf. Ser. 376, *Astronomical Data Analysis Software and Systems XVI*, ed. R. A. Shaw, F. Hill, & D. J. Bell (San Francisco, CA: ASP), 127
 Meidt, S. E., Hughes, A., Dobbs, C. L., et al. 2015, *ApJ*, **806**, 72
 Meidt, S. E., Schinnerer, E., García-Burillo, S., et al. 2013, *ApJ*, **779**, 45
 Menon, S. H., Grasha, K., Elmegreen, B. G., et al. 2021, *MNRAS*, **507**, 5542
 Messa, M., Adamo, A., Calzetti, D., et al. 2018, *MNRAS*, **477**, 1683
 Messa, M., Calzetti, D., Adamo, A., et al. 2021, *ApJ*, **909**, 121
 Miville-Deschênes, M.-A., Murray, N., & Lee, E. J. 2017, *ApJ*, **834**, 57
 Nayak, O., Meixner, M., Indebetouw, R., et al. 2016, *ApJ*, **831**, 32
 Nguyen, N. K., Pettitt, A. R., Tasker, E. J., & Okamoto, T. 2018, *MNRAS*, **475**, 27
 Peters, W. L., Freeman, K. C., Forster, J. R., Manchester, R. N., & Ables, J. G. 1994, *MNRAS*, **269**, 1025
 Pettitt, A. R., Dobbs, C. L., Baba, J., et al. 2020, *MNRAS*, **498**, 1159
 Pettitt, A. R., Egusa, F., Dobbs, C. L., et al. 2018, *MNRAS*, **480**, 3356
 Qing, G., Wang, W., Liu, J.-F., & Yoachim, P. 2015, *ApJ*, **799**, 19
 Querejeta, M., Schinnerer, E., Meidt, S., et al. 2021, *A&A*, **656**, A133
 Radburn-Smith, D. J., de Jong, R. S., Seth, A. C., et al. 2011, *ApJS*, **195**, 18
 Rice, T. S., Goodman, A. A., Bergin, E. A., Beaumont, C., & Dame, T. M. 2016, *ApJ*, **822**, 52
 Rosolowsky, E., Hughes, A., Leroy, A. K., et al. 2021, *MNRAS*, **502**, 1218
 Rosolowsky, E. W., Pineda, J. E., Kauffmann, J., & Goodman, A. A. 2008, *ApJ*, **679**, 1338
 Sabbi, E., Calzetti, D., Ubeda, L., et al. 2018, *ApJS*, **235**, 23
 Schinnerer, E., Meidt, S. E., Pety, J., et al. 2013, *ApJ*, **779**, 42
 Sidorin, V., 2017 Quickclump: Identify clumps within a 3D FITS datacube, *Astrophysics Source Code Library*, ascl:1704.006
 Silva-Villa, E., Adamo, A., & Bastian, N. 2013, *MNRAS*, **436**, L69
 Silva-Villa, E., & Larsen, S. S. 2012, *MNRAS*, **423**, 213
 Solomon, P. M., Rivolo, A. R., Barrett, J., & Yahil, A. 1987, *ApJ*, **319**, 730
 Stanghellini, L., Magrini, L., & Casasola, V. 2015, *ApJ*, **812**, 39
 Sun, J., Leroy, A. K., Rosolowsky, E., et al. 2022, *AJ*, **164**, 43
 Sun, J., Leroy, A. K., Schinnerer, E., et al. 2020, *ApJL*, **901**, L8
 Sun, J., Leroy, A. K., Schrubba, A., et al. 2018, *ApJ*, **860**, 172
 Turner, J. A., Dale, D. A., Lilly, J., et al. 2022, *MNRAS*, **516**, 4612
 Virtanen, P., Gommers, R., Oliphant, T. E., et al. 2020, *NatMe*, **17**, 261
 Wainer, T. M., Johnson, L. C., Seth, A. C., et al. 2022, *ApJ*, **928**, 15
 Walker, D. L., Longmore, S. N., Zhang, Q., et al. 2018, *MNRAS*, **474**, 2373
 Walsh, J. R., & Roy, J. R. 1997, *MNRAS*, **288**, 726
 Whitmore, B. C., Chandar, R., Lee, J. C., et al. 2023, *MNRAS*, **520**, 63
 Wong, T., Hughes, A., Ott, J., et al. 2011, *ApJS*, **197**, 16
 Wong, T., Oudshoorn, L., Sofovitch, E., et al. 2022, *ApJ*, **932**, 47
 Yu, S.-Y., Ho, L. C., & Wang, J. 2021, *ApJ*, **917**, 88